THE JOURNAL OF PHYSICAL CHEMISTRY B

Article

Cite This: J. Phys. Chem. B 2018, 122, 11771−11783

pubs.acs.org/JPCB

Modeling the Self-Assembly of Protein Complexes through a Rigid-Body Rotational Reaction−Diffusion Algorithm

Margaret E. Johnson*

TC Jenkins Department of Biophysics, The Johns Hopkins University, 3400 North Charles Street, Baltimore, Maryland 21218, United States

Supporting Information

ABSTRACT: The reaction−diffusion equations provide a powerful framework for modeling nonequilibrium, cell-scale dynamics over the long time scales that are inaccessible by traditional molecular modeling approaches. Single-particle reaction−diffusion offers the highest resolution technique for tracking such dynamics, but it has not been applied to the study of protein self-assembly due to its treatment of reactive species as single-point particles. Here, we develop a relatively simple but accurate approach for building rigid structure and rotation into single-particle reaction−diffusion methods, providing a rate-based method for studying protein self-assembly. Our simplifying assumption is that reactive collisions can be evaluated purely on the basis of the separations between the sites, and not their orientations. The challenge of evaluating reaction probabilities can then be performed using well-known equations based on translational diffusion in both 3D and 2D, by employing an effective diffusion constant we derive here. We show how our approach reproduces both the kinetics of association, which is altered by rotational diffusion, and the equilibrium of reversible association, which is not. Importantly, the macroscopic kinetics of association can be predicted on the basis of the microscopic parameters of our structurally resolved model, allowing for critical comparisons with theory and other rate-based simulations. We demonstrate this method for efficient, rate-based simulations of self-assembly of clathrin trimers, highlighting how formation of regular lattices impacts the kinetics of association.

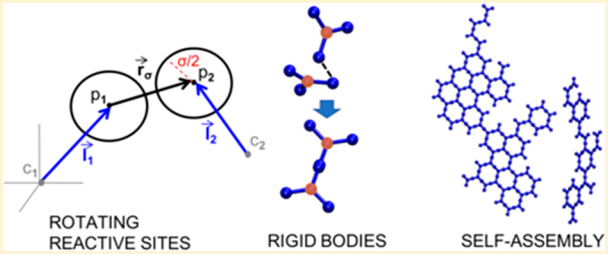

1. INTRODUCTION

Multiprotein self-assembly is a critical step in a diverse array of cellular pathways, including vesicle trafficking,[1,2] signal transduction,[3] and viral bud formation.[4] Computer simulations of self-assembly such as viral capsid dynamics,[5−11] crystal forming polyhedra,[12] and DNA building blocks[13] provide detailed insights into mechanisms, kinetics, and stability of assembly formations. In clathrin-mediated endocytosis, the assembly of the clathrin lattice,[14] which we simulate here, is a driving force for vesicle formation. Computer simulations have revealed critical roles of clathrin structure,[15] clathrin-adaptor structure,[16,17] membrane stiffness,[18,19] and nonspecific interactions between clathrin trimers[20] in reproducing both ordered and disordered clathrin assemblies.

Standard computational approaches for self-assembly use molecular dynamics,[21] Monte Carlo,[22] or Brownian dynamics with potential-based interactions (e.g., see refs 23−28). With these more commonly used energy-function-based approaches, however, nonequilibrium events such as protein production and external energy sources cannot be modeled. Moreover, the coarse-graining[5,9,29] necessary to reach the seconds time scale prevents the incorporation of chemical transformations such as phosphorylation. Rate-based approaches, such as the one we develop here, offer an attractive alternative to energy-function-based approaches because they can readily capture kinetics of general nonequilibrium systems over long time scales.

Rate-based approaches, such as ordinary (ODE) or partial differential equations (PDEs) and stochastic simulations (spatial or nonspatial/Gillespie[30,31]), are well-established for studying cellular dynamics. These methods solve well-defined equations of motion and utilize experimentally measured rates for binding interactions or chemical reactions, facilitating studies of complex biochemical networks,[32] for example. However, self-assembly presents new challenges[33] and has almost exclusively been modeled with either ODEs or Gillespie simulations, which lack any spatial or structural resolution[34−36] (although heuristic spatial treatments exist[37]). These rule-based simulations[38−40] are efficient and powerful,[34,40−43] but without spatial or geometric constraints, they cannot capture the impact of sterics, excluded volume, diffusion, or spatial localization. The spatially resolved approaches such as continuous (PDEs)[44,45] or lattice-based[46−49] simulators lack particle (molecular) resolution, preventing their application to structure-resolved self-assembly.

Single-particle reaction−diffusion (RD) methods[50−56] provide a natural starting point for building structure into a spatially resolved, rate-based approach. While not yet generally

Special Issue: William A. Eaton Festschrift

Received: August 27, 2018
Revised: September 25, 2018
Published: September 26, 2018

DOI: 10.1021/acs.jpcb.8b08339
J. Phys. Chem. B 2018, 122, 11771−11783

developed for self-assembly, single-particle RD simulations have provided mechanistic insight into diverse cellular processes,[52,57−60] including a study of self-assembly of receptor clusters on 2D lattices.[61] The most versatile algorithm, brute-force Brownian dynamics (BD) with reactive collisions, has already been used to study association of rotating and translating rigid molecules that can orient and interact via potentials.[62−66] However, because BD is only accurate if very short time steps (femtosecond to picosecond) are used when particles approach contact, it is inefficient and usually restricted to simulations of two proteins. When BD is used within multiscale methods,[67] larger systems can be studied, but BD still represents a rate-limiting step in the simulations. Here, we consider as a starting point for our approach the recent single-particle methods developed to enable relatively large time steps (nanosecond to millisecond) while preserving RD dynamics. They generally fall into two classes, the kinetic Monte Carlo (KMC) approaches,[54,55] which preserve the macroscopic kinetics of association, and the more microscopic Green's-function (GF)-based approaches, which are derived from the Smoluchowski model.[68] Of the GF approaches, the GFRD algorithm preserves exact dynamics of RD equations,[52,69,70] Smoldyn produces approximate rate behavior,[56,71,72] and the free-propagator reweighting (FPR) algorithm we use here preserves exact rates and long-range dynamics of RD equations.[50,51]

The primary reason single-particle RD has not been used for self-assembly is that any departure from simple translational diffusion makes it exceedingly difficult to accurately propagate both dynamics and binding reactions between particles. In general, adding in free rotational diffusion to rigid bodies is not difficult. The major challenge is to evaluate the reaction probabilities that such species will react upon collision. Reaction probabilities differ for KMC methods versus GF-based methods, but they are ultimately calculated on the basis of analytical equations that are only available for translationally diffusing particles with spherical reactive boundaries. Thus, the goal of our approach here is to derive a method for efficiently and accurately evaluating reaction probabilities for RD models that extend from a single site to a multisite molecule undergoing rotation as a rigid body. We achieve this goal by allowing reactions to occur at any molecular orientations, and then defining an effective diffusion constant, D_{eff}, that allows us to evaluate reaction probabilities using well-known solutions to the translation-only RD equation.[73,74] We note that the Spring SALAD method[75] is similar to our model in that it connects multiple spherical sites into one molecule, using harmonic springs rather than rigid-body dynamics. This requires a smaller time step to propagate dynamics but could similarly be integrated with our approach here.

To briefly introduce our model, we have moved beyond spherical particles by defining a protein as a series of spherical interaction sites connected in a rigid geometry (Figure 1). Reactions occur at a specific collision distance σ, irrespective of orientation of the two proteins. Because reactions are independent of molecular orientation, a limitation of our approach is that binding events produce complexes with arbitrary geometries. In our method, we must therefore enforce any desired orientation after binding occurs. This artificial "snapping" into place of the binding partners upon association violates the governing equation of motion for the sites, as discussed further below. However, we consider this trade-off of orientational dynamics for structure to be justified for two

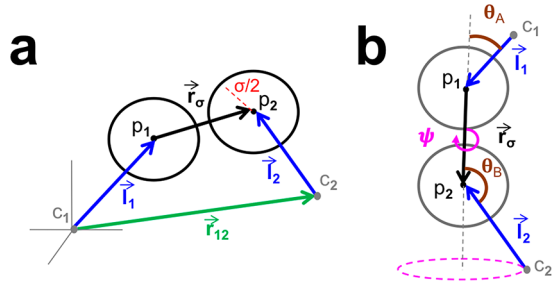

Figure 1. Schematic of the model of two rigid proteins. (A) Each protein here has a single reactive particle p_i (i = 1 or 2) connected rigidly to a central, nonreactive site c_i that undergoes purely translational diffusion. The "leg" vectors $\mathbf{l}_1$ and $\mathbf{l}_2$ (blue) undergo purely rotational diffusion. Reactions occur when the reactive particles collide, at $r_\sigma = \sigma$. (B) The solution to this model can be solved numerically as a function of the separation r_σ and three relative angles: the dihedral angle ψ (pink) of $\mathbf{l}_1$ relative to $\mathbf{l}_2$, and the polar angles θ_A and θ_B (brown) of $\mathbf{l}_1$ and $\mathbf{l}_2$ relative to the vector $\mathbf{r}_\sigma$.

reasons. First, we can quantitatively compare the microscopic kinetics produced by our model (dependent on k_a, k_b, σ, D_1, D_2, D_{R1}, D_{R2}, and leg lengths l_1 and l_2) with the macroscopic kinetics of rate equations and experimental measurements (k_{on} and k_{off}). This facilitates ready comparison between our model and other simulations and experiments. Second, we are able to simulate thousands of molecules interacting over minutes or longer time scales. These simulations are the first to the authors' knowledge for modeling self-assembly with a spatially resolved rate-based method.

In this paper, we first provide background on single-particle RD before deriving an effective diffusion constant D_{eff} for capturing single-particle rotational and translation diffusion. We then demonstrate how this general theoretical approximation can be used particularly well in GF-based methods for efficient and accurate solutions to pairwise association. We calculate exact numerical solutions of reaction probabilities from full rotational and translational reaction−diffusion simulations using BD simulations[64] to test our approximate reaction probabilities that use D_{eff}. We provide validation for many-body simulations of rotating and translating sites at equilibrium, and their full time-dependent kinetics using Smoluchowski theory,[68] where rates are calculated from numerical BD simulations.[64,65] We validate the method in 3D and in 2D, where the kinetics of association are much more sensitive to spatial considerations.[51] Lastly, we illustrate the potential of this method by simulating rigid-body assembly of clathrin trimers, modeled here as three-site rigid bodies. We compare and contrast our results with the lower resolution rate-based Gillespie simulations[30] with rule-based species tracking.[38] We discuss the portability of this approach to other single-particle methods and spell out steps needed to use it in these other methods. Overall, this method provides a framework for nonequilibrium simulations of self-assembly in the cell, which can be coupled to other rate-based reactions.

2. THEORY

2.1. Smoluchowski Model for Single-Particle Reaction−Diffusion. *Background.* Before describing our model (Figure 1), it is necessary to provide background on the Smoluchowski model.[68] Point particles obey diffusive dynamics. For a pair of particles, 1 and 2, the reaction is entirely dependent on the separation between the two particles, and

DOI: 10.1021/acs.jpcb.8b08339
J. Phys. Chem. B 2018, 122, 11771−11783

reactions occur upon collision at the binding radius σ with an intrinsic reaction rate k_a (due to Collins and Kimball[76]). The net diffusion is solely due to translational diffusion,

$$D_{tot} = D_1 + D_2 \tag{1}$$

with translational diffusion constants always notated with subscript 1, 2, or t. The separation r between the particle pair with initial separation $r = r_0$ at time zero obeys the diffusion equation,

$$\frac{\partial p(r,t|r_0)}{\partial t} = D_{tot}\frac{1}{r^{d-1}}\frac{\partial}{\partial r}\left(r^{d-1}\frac{\partial p(r,t|r_0)}{\partial r}\right) \tag{2a}$$

where d is the dimensionality and $p(r,t|r_0)$ is the probability of finding the particles separated by r at time t. The reactive boundary at $r = \sigma$ is modeled via the radiation boundary condition (RBC)[76]

$$D_{tot}\frac{\partial p(r,t|r_0)}{\partial r}\bigg|_{r=\sigma} = \kappa p(\sigma,t|r_0) \tag{2b}$$

where $\kappa = k_a/B(\sigma,d)$. In 2D the boundary region $B(\sigma,d=2) = 2\pi\sigma$, and in 3D, $B(\sigma,d=3) = 4\pi\sigma^2$. The other boundary condition is

$$p(r=\infty,t|r_0) = 0 \tag{2c}$$

and the initial condition is a delta function,

$$p(r,t=0|r_0) = \delta(r - r_0)/B(\sigma,d) \tag{2d}$$

The Green's function (GF) solution to eq 2, which we will denote as $p_{irr}(r,t|r_0)$ for irreversible association, can be solved analytically for this model.[74] However, once rotation, orientation, or forces are introduced, as we do below with rotation, the model can only be solved numerically.

The central challenge of propagating single-particle reaction diffusion is defining the probability of a reaction occurring between two particles that have collided or may, in the next time step, collide with one another. For the Smoluchowski model, there is a rigorous definition of the reaction probability for association, p_{react}, which is the complement of the survival probability S, the integral over the GF. The probability of a reaction occurring in a time t given an initial separation r_0 is thus given by

$$S(t|r_0) = \int_\sigma^\infty \mathrm{d}\mathbf{r}\, p_{irr}(r,t|r_0) \tag{3a}$$

$$p_{react}(t|r_0) = 1 - S(t|r_0) \tag{3b}$$

Through the GF, the reaction probabilities depend on the parameters k_a, D_1, D_2, and σ. The functional forms of these probabilities are known analytically in all three dimensions[74] and analyzed elsewhere (see, e.g., 3D[50] and 2D[51]).

Dissociation in microscopic models is independent of the dynamics of the particles and is controlled by the intrinsic dissociation rate, k_b (s^{-1}). It can be accurately modeled as a Poisson process, where

$$p_{dissoc}(t) = 1 - \exp(-k_b t) \tag{4}$$

For the Smoluchowski model, association occurs upon collision, where $r = \sigma$. To ensure detailed balance, dissociation events must return particles back to contact, $r = \sigma$.

Macroscopic vs Microscopic Rates. One can directly compare the microscopic kinetics (dependent on k_a, k_b, σ, D_1, D_2) with the macroscopic kinetics of rate equations and experimental measurements (k_{on}, k_{off}). The macroscopic rate from the Smoluchowski model is a function of time and is related to the survival probability (eq 3a) via[65]

$$k(t) = k_a S(t|\sigma) \tag{5}$$

For binding reactions (A + B) in solution (3D), the time-dependent rate reaches a steady state rate given by[73]

$$k_{on}^{3D} = \left(\frac{1}{k_a^{3D}} + \frac{1}{4\pi D_{tot}\sigma}\right)^{-1} \tag{6}$$

and the equilibrium is preserved for microscopic and macroscopic rates in 2D and 3D:

$$K_q = \frac{k_{on}}{k_{off}} = \frac{k_a}{k_b} \tag{7}$$

In 2D (on surfaces), unlike in 3D, there is no steady-state rate, due to the fundamental properties of diffusion in 2D (the critical dimension) versus 3D. We previously derived regimes to establish when a steady-state rate is a valid approximation and defined an optimal value for k_{on}^{2D}.[51] See the Methods for adjustment for self-binding (A + A).

2.2. Model for Single-Particle Reaction–Diffusion with Rotating Sites. Our model here (Figure 1) differs from previous work on particles undergoing rotational and translational diffusion[64,66,77,78] because we have added the second center of mass site, and we do not place orientational constraints on reactions. We consider a reactive particle $\mathbf{p}_1$ that is connected to a nonreactive center position $\mathbf{c}_1$ through a rigid arm, $\mathbf{l}_1 = \mathbf{p}_1 - \mathbf{c}_1$. Similarly, reactive particle $\mathbf{p}_2$ is connected to its center position $\mathbf{c}_2$ through a rigid arm, $\mathbf{l}_2 = \mathbf{p}_2 - \mathbf{c}_2$. The lengths of both arms, l_1 and l_2, do not change. Reactions occur along the vector separating the reactive particles, $\mathbf{r}_\sigma = \mathbf{p}_2 - \mathbf{p}_1$. The dynamics of $\mathbf{r}_\sigma$ depends on the translational diffusion of the centers and the rotational diffusion of the legs, since

$$\mathbf{r}_\sigma = \mathbf{r}_{12} + \mathbf{l}_2 - \mathbf{l}_1 \tag{8}$$

The model is parametrized by the familiar parameters for the Smoluchowski model of k_a, D_1, D_2, and σ, as well as four additional rotational parameters: D_{R1}, D_{R2}, l_1, and l_2.

The equation of motion can be defined on the basis of the purely translational diffusion of the centers $\mathbf{c}_1$ and $\mathbf{c}_2$, and the purely rotational diffusion of $\mathbf{l}_1$ and $\mathbf{l}_2$. The diffusion of the centers relative to one another, $\mathbf{r}_{12} = \mathbf{c}_2 - \mathbf{c}_1$ obeys the translational diffusion equation with $D_{tot} = D_1 + D_2$, such that, similar to previous work,[64] we can write

$$\frac{\partial p(\mathbf{r}_{12},\mathbf{l}_1,\mathbf{l}_2,t|\mathbf{r}_{120},\mathbf{l}_{10},\mathbf{l}_{20})}{\partial t} = (D_{tot}\nabla_{12}^2 + D_{R1}\nabla_{\omega 1}^2 + D_{R2}\nabla_{\omega 2}^2)p \tag{9a}$$

The Laplacian for the translational diffusion of a vector $\mathbf{r}$ with length r, polar angle θ, and azimuth φ in spherical coordinates is given by $\nabla^2 = \frac{1}{r^2}\frac{\partial}{\partial r}\left(r^2\frac{\partial}{\partial r}\right) + \frac{1}{r^2}\nabla_\omega^2$, where $\nabla_\omega^2 = \frac{1}{\sin\theta}\frac{\partial}{\partial\theta}\left(\sin\theta\frac{\partial}{\partial\theta}\right) + \frac{1}{\sin^2\theta}\frac{\partial^2}{\partial^2\varphi}$. Reactions are introduced as usual via the RBC applied along the vector separating the reactive particles, which for this model is $\mathbf{r}_\sigma = \mathbf{p}_2 - \mathbf{p}_1$. Reactive collisions occur at $r_\sigma = \sigma$, independently of the orientations of $\mathbf{l}_1$ and $\mathbf{l}_2$. The flux along $\mathbf{r}_\sigma$ at the separation σ is proportional to the density at σ, giving

DOI: 10.1021/acs.jpcb.8b08339
J. Phys. Chem. B 2018, 122, 11771–11783

$$-\mathbf{J}\cdot\hat{\mathbf{r}}_\sigma|_{r_\sigma=\sigma} = \kappa p(r_\sigma=\sigma,t|\boldsymbol{r}_{120},\boldsymbol{l}_{10},\boldsymbol{l}_{20}) \quad (9b)$$

where the flux is given by $\mathbf{J} = -(D_{\mathrm{tot}}\nabla_{12} + l_1 D_{\mathrm{R1}}\nabla_{\mathrm{rot1}} + l_2 D_{\mathrm{R2}}\nabla_{\mathrm{rot2}})p(\mathbf{r}_{12},\mathbf{l}_1,\mathbf{l}_2,t|\mathbf{r}_{120},\mathbf{l}_{10},\mathbf{l}_{20})$ and where $\nabla = \hat{\mathbf{r}}\frac{\partial}{\partial r} + \frac{1}{r}\nabla_{\mathrm{rot}}$ and $\nabla_{\mathrm{rot}} = \hat{\boldsymbol{\theta}}\frac{\partial}{\partial\theta} + \hat{\boldsymbol{\varphi}}\frac{1}{\sin(\theta)}\frac{\partial}{\partial\varphi}$. Similar to eq 2, the same large-separation BC applies (eq 2c) and the same delta function initial conditions are used for each variable (eq 2d). In the limit of no rotational motion ($D_{\mathrm{R1}} = D_{\mathrm{R2}} = 0$, or $l_1 = l_2 = 0$), this model (eq 9) simplifies back to the purely translational result of eq 2.

Generally, the full model (eq 9) cannot be solved analytically because the RBC is along $\mathbf{r}_\sigma$ and this vector depends on both translational and rotational diffusion. To simplify our numerical calculations performed with BD simulations,[65] we can redefine the GF as a function of fewer variables, as illustrated in Figure 1b, given that it is only the relative separation and orientations of the molecules that affects their collision probability. Thus, the GF becomes $p_{\mathrm{irr,rot}}(r_\sigma,\theta_{\mathrm{A}},\theta_{\mathrm{B}},\psi,t|r_{\sigma 0},\theta_{\mathrm{A}0},\theta_{\mathrm{B}0},\psi_0)$; it is a function of the separation r_σ, the angle of each leg vector relative to $\mathbf{r}_\sigma$: $\theta_{\mathrm{A}} = \mathrm{acos}[\mathbf{r}_\sigma\cdot\mathbf{l}_1/(r_\sigma l_1)]$, and $\theta_{\mathrm{B}} = \mathrm{acos}[\mathbf{r}_\sigma\cdot\mathbf{l}_2/(r_\sigma l_2)]$, and the dihedral angle between the leg vectors $\psi = \mathrm{acos}[\mathbf{n}_1\cdot\mathbf{n}_2/(n_1 n_2)]$, where $\mathbf{n}_1 = \mathbf{r}_\sigma\times\mathbf{l}_1$ and $\mathbf{n}_2 = \mathbf{r}_\sigma\times\mathbf{l}_2$. The survival probability and reaction probability for this full rotational and translational GF is

$$S_{\mathrm{rot}}(\Delta t|r_{\sigma 0},\theta_{\mathrm{A}0},\theta_{\mathrm{B}0},\psi_0) = \int_\sigma^\infty \mathrm{d}\mathbf{r}_\sigma \int_{-1}^1 \mathrm{d}\cos(\theta_{\mathrm{A}}) \int_{-1}^1 \mathrm{d}\cos(\theta_{\mathrm{B}}) \times \int_0^{2\pi} \mathrm{d}\psi\, p_{\mathrm{irr,rot}}(r_\sigma,\theta_{\mathrm{A}},\theta_{\mathrm{B}},\psi,\Delta t|r_{\sigma 0},\theta_{\mathrm{A}0},\theta_{\mathrm{B}0},\psi_0) \quad (10a)$$

$$p_{\mathrm{react,rot}}(\Delta t|r_{\sigma 0},\theta_{\mathrm{A}0},\theta_{\mathrm{B}0},\psi_0) = 1 - S_{\mathrm{rot}}(\Delta t|r_{\sigma 0},\theta_{\mathrm{A}0},\theta_{\mathrm{B}0},\psi_0) \quad (10b)$$

2.3. Derivation of Effective Diffusion Constant D_{eff} for Describing Translational and Rotational Diffusion.

When a site with arm length l_1 and rotational diffusion constant D_{R1} rotates over a time step Δt, it sweeps out an average squared angular displacement (Figure 2) of

$$\langle\omega^2(\Delta t)\rangle = 2(d-1)D_{\mathrm{R1}}\Delta t \quad (11)$$

where

$$\omega(t) = \mathrm{acos}(\mathbf{l}_1(t)\cdot\mathbf{l}_1(0)/l_1^2) \quad (12)$$

and d is the dimensionality. Using the law of cosines, the average squared Cartesian distance traveled over this angular displacement is then

$$\Delta r_1^2(\Delta t) = 2l_1^2(1-\cos(\sqrt{\langle\omega^2(\Delta t)\rangle}) \quad (13)$$

Using the familiar Einstein relation, we can then define a translational diffusion constant that would produce this squared displacement as

$$D_{1,\mathrm{rot,diff}} \approx \Delta r_1^2(\Delta t)/2d\Delta t \quad (14)$$

The same calculation applies to $\mathbf{p}_2$. We approximate net diffusion along r_σ as the sum of the particles' translational diffusion constants and these contributions from rotational diffusion (eq 14), producing the main result:

$$D_{\mathrm{eff}}(\Delta t) = D_1 + D_2 + \frac{\Delta r_1^2 + \Delta r_2^2}{2d\Delta t} \quad (15)$$

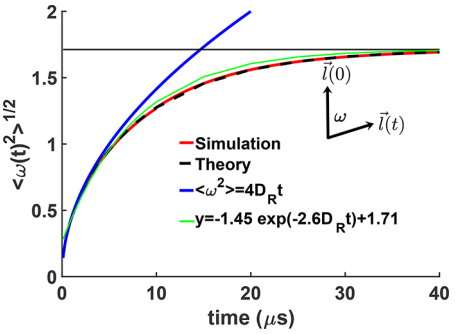

Figure 2. Mean squared angular displacements (MSAD) from purely rotational diffusion of a vector $\mathbf{l}$ is known over all time scales and values of D_{R}. The expected result (blue) ignores the periodicity of rotation, and we are interested in the Cartesian displacement $|\mathbf{l}(t) - \mathbf{l}(0)|^2$ after a time t. With ω (see inset) thus limited to the range $0{:}\pi$, the MSAD can be calculated from eq 16 (black dashed), with the asymptotic value reached upon uniform sampling shown in solid black. We found a reasonable fit shown in the green curve (eq 18) to simplify calculations of $\langle\omega^2(t)\rangle^{1/2}$. Our simulations of free rotational diffusion using Euler angle updates (red) correctly sample the exact solution (black dashed).

This approximation produces the correct limiting behavior: as either $l_{1,2} \to 0$ or $D_{\mathrm{R1,2}} \to 0$, rotation no longer influences reactions and the purely translational result is recovered.

Since D_{eff} depends on the size of $\langle\omega^2(t)\rangle^{1/2}$, we note that eq 11 ignores the periodicity of rotation. As far as net Cartesian displacement is concerned (eq 13), rotation of 2π is the same as 4π. Thus, when angular displacements are limited to between 0 and π, eq 11 works well up to $\langle\omega^2(t)\rangle^{1/2} \sim <1$ rad (Figure 2). We can derive the squared angular displacement

$$\langle\omega^2(t)\rangle = \langle\theta^2(t)|\theta_0{=}0\rangle = 2\pi\int_0^\pi \sin(\theta)\,\mathrm{d}\theta\,\theta^2 p_{\mathrm{free,rot}}(\theta,t|\theta_0{=}0) \quad (16)$$

using the well-known solution for free rotational diffusion,

$$p_{\mathrm{free,rot}}(\theta,\varphi,t|\theta_0,\varphi_0) = \sum_{l=0}^\infty \sum_{m=-l}^{l} Y_l^{m*}(\theta_0,\varphi_0)\, Y_l^m(\theta,\varphi)\mathrm{e}^{-tD_{\mathrm{R}}l(l+1)} \quad (17)$$

given delta function initial conditions $p(\theta,\varphi,t{=}0|\theta_0,\varphi_0) = \delta(\theta-\theta_0)\,\delta(\varphi-\varphi_0)$. With an initial polar angle of $\theta_0 = 0$, the resulting distribution will be uniform in φ. At long times the distribution becomes uniform in θ, and the asymptotic value is $\langle\omega^2(\infty)\rangle = \frac{\pi^2-4}{2}$ in 3D and $\pi^2/3$ in 2D. We numerically solved eq 16 over all other times (Figure 2 black dashed). We also found a reasonable global fit for values where $\langle\omega^2(t)\rangle^{1/2} > 1$ rad and eq 11 does not apply, on the basis of comparing fits across several different values of D_{R}. In 3D,

$$\langle\omega^2(t)\rangle^{1/2} \approx -1.45\exp(-2.6D_{\mathrm{R}}t) + \langle\omega^2(\infty)\rangle^{1/2}_{\mathrm{3D}} \quad (18a)$$

and in 2D,

$$\langle\omega^2(t)\rangle^{1/2} \approx -1.5\exp(-1.2D_{\mathrm{R}}t) + \langle\omega^2(\infty)\rangle^{1/2}_{\mathrm{2D}} \quad (18b)$$

We demonstrate in Figure 3 that our assumption that rotational dynamics can be approximately captured by D_{eff} works well. The mean squared Cartesian displacement (MSD)

DOI: 10.1021/acs.jpcb.8b08339
J. Phys. Chem. B 2018, 122, 11771−11783

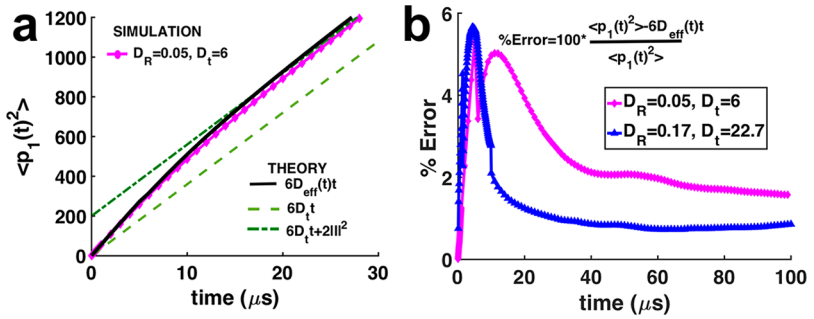

Figure 3. (a) Mean squared displacement (MSD) of a translating and rotating molecular site (pink) described by D_{eff} (black). Simulations of a point p_1 located l = 10 nm from the center of mass have no reactions occur (pink). The expected MSD from the Einstein relation, $\langle|\mathbf{p}_1(t) - \mathbf{p}_1(0)|^2\rangle = 6D_t$, is shown for $D = D_t$ in dashed green, and in dark green the intercept is offset by the maximum rotational distance of $2l^2$. We calculate $D_{eff}(t)$ using eq 15, where $\langle\omega^2(t)\rangle^{1/2}$ is given by $4D_R t$ up to 1 rad, and otherwise is calculated via eq 18. Percent error between the simulated results and the theoretical prediction using $D_{eff}(t)$ is shown for (a) as well as for a simulation with the same leg length but faster diffusion.

of a single particle $\mathbf{p}_1$ undergoing free translational and rotational diffusion is calculated from simulation. At short times (<∼10 μs), the slope is steeper than expected from purely translational diffusion, due to the effects of rotation. At longer times, however, the slope of the MSD is again described by the translational diffusion constant only, as rotation can maximally contribute a net displacement of $2l^2$. The simulation data are well described by the use of the Einstein relation with D_t replaced by $D_{eff}(t)$ (eq 15).

3. METHODS

3.1. Simulation Algorithm Outline. On the basis of the theory above, we outline here a general stepwise implementation for association of pairs.

1. Given an instantaneous configuration, calculate the separation r between pairs of reactive sites.
2. For each reactive pair, calculate their effective diffusion constant D_{eff} using eq 15.
3. For each reactive pair, calculate p_{react} (using, e.g., eq 3b), given the time step, the current particle separation r, and the reaction parameters: k_a, σ, and D_{eff}.
4. (A) If p_{react} > URN, move sites to contact and "snap" them into place.
   (B) Else, sample Brownian displacements (rotational and translational) for both molecules (Supporting Information), and reject moves that create overlap between pairs ($r < \sigma$).

We note that any specific method may have minor modifications from this procedure. For the FPR method, for example, in step 3, we would also need to calculate and apply reweighting ratios to the reaction probabilities. Time steps should also be chosen such that, on average, only pairs of molecule could react in each step.[50]

3.2. Simulation Details for Many-Body Rotational FPR. All many-body simulations used the FPR algorithm.[50,51] Rigid molecules were initialized in the unbound state and positioned randomly in a box. Reactive sites were prevented from overlapping. Box lengths were 494 nm in x, y, and z unless otherwise indicated, and 2D simulations were restricted to the x−y plane. Reflective boundary conditions were used for the box boundaries; sites that diffused out of the box were placed back inside by the displaced amount. Diffusion constants for complexes were slowed on the basis of the growth in the hydrodynamic radius (Supporting Information). For each system, at least 20 trajectories (N_{traj}) were collected, and the standard error of the mean (SEM) for a variable x was calculated at each time point using $\mathrm{SEM}(t) = \langle(x(t) - \langle x(t)\rangle)^2\rangle^{1/2}/\sqrt{N_{traj}}$.

For self-binding reactions (A + A), we note that the relationship between macroscopic and microscopic rates (eq 6) is instead given by $k_{on}^{3D} = \frac{1}{2}\left(\frac{1}{k_a^{3Dself}} + \frac{1}{4\pi D_{tot}\sigma}\right)^{-1}$, and eq 7 is $K_{eq} = \frac{k_{on}}{k_{off}} = \frac{k_a^{self}}{2k_b}$ in 3D and 2D. These relationships are needed to define the k_a and k_b values for direct comparison to the Gillespie simulations that use k_{on} and k_{off}.

For clathrin trimer simulations, when association occurs, molecules are translated to contact and then rotated into a predefined planar orientation. This new structure is then tested to check if the association has produced overlap between clathrin trimers in a lattice, which can happen if larger structures bind. If so, the event is rejected and both complexes are returned to their position prior to association. When dissociation occurs, two complexes are created and a tree search is used to maintain the bonded structure within each new complex. Reactive sites stay at contact following dissociation. If a "bond" dissociates within a closed hexagon, the complex remains as a single unit, with the reactive sites now "freed" to rebind. We note that for these simulations, when reactive sites are in a bound state, they do not enforce excluded volume. While maintaining excluded volume of both free and bound sites is straightforward, we chose not to do it here simply to speed up the simulations. To simulate 30 s of real time took ∼14 h on one CPU. For further details on the FPR method, the BD simulations, and the Gillespie simulations; see Supporting Information.

4. RESULTS

4.1. Reaction Probabilities and GFs for Rotating Sites Approximated through the Use of D_{eff}. The correct reaction probability for association for our model of Figure 1 is given by eq 10b, which is not analytically soluble. We find that using $D_{tot} = D_{eff}$ in the solutions to the model of eq 2 does an excellent job of describing the orientationally averaged solutions from the full model. We illustrate the results with a diffusion-controlled reaction (k_a = 166.9 nm^3/μs = 1.01 × 10^8 M^{-1} s^{-1}), to maximize the sensitivity of the model to changes in diffusion. In Figure 4 we plot the survival probabilities of association for the full model (eq 10a) as a function of initial separation of the pairs $r_{\sigma 0}$, and initial orientation of the legs, Ω_0

DOI: 10.1021/acs.jpcb.8b08339
J. Phys. Chem. B 2018, 122, 11771−11783

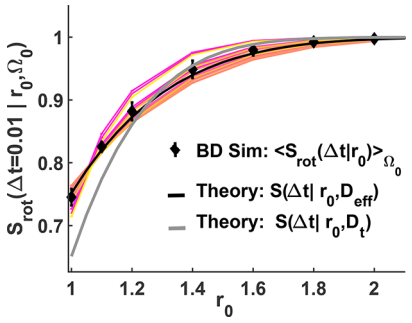

Figure 4. Survival probabilities of association for two rotating and translating reactive particles are accurately approximated by use of D_{eff}. Each colorful curve is the survival probability (calculated numerically from BD simulations (Supporting Information)) between p_1 and p_2 over time $\Delta t = 0.01$ μs given an initial separation $r_\sigma = r_0$ in nm, and an initial orientation $\Omega_0 = [\theta_{A0}, \theta_{B0}, \psi_0]$ (eq 10a). The black diamonds are the average over all initial orientations. Error bars are standard deviations across all angles. Both theory curves show the survival probability predicted from the simpler analytical model (eq 3a), which depends only on the initial separations of the particles, r_0. Both particles rotate with $D_R = 0.05$ rad$^2/\mu$s and with l = 10 nm. One molecule has $D_1 = 0$, the other has $D_2 = 6$ nm$^2/\mu$s, thus $D_t = D_2$. We calculate D_{eff} from eq 15 with the time step $\Delta t = 0.01$ μs, giving $D_{eff} = 12.66$ nm$^2/\mu$s. The rate is $k_a = 166.9$ nm$^3/\mu$s and $\sigma = 1$ nm.

$= [\theta_{A0}, \theta_{B0}, \psi_0]$. Although there is clearly a dependence on the initial orientation of the legs, it is relatively small. This is because, while orientation affects the path swept out by the rotation of the particles, reactions occur upon any collision, independently of the molecules' orientation. Critically, once initial orientations have been averaged over, we confirm that the resulting survival probabilities are well described by $S(t|r_0,D_{eff})$ of eq 3a. In contrast, the agreement is clearly worse for $S(t|r_0,D_t)$. In Figure 5 we show that, similarly, the orientationally averaged GF solutions to eq 9 are also well described by the solutions to eq 2 when $D_{tot} = D_{eff}$. Here again, if we ignore the effect of rotation and use $D_{tot} = D_t$, the agreement is much worse. The trend is the same whether we solve for the full model including RBC (Figure 5a), or we solve for free diffusion (no reactions) (Figure 5b). Interestingly, the ratio of these two GFs (Figure 5c) is rather insensitive to the value of D_{tot} used. This ratio is used for reweighting in the FPR simulations (see Methods).

4.2. Time-Dependent Rates of Association Captured by D_{eff}. The macroscopic rates of association (k_{on}, k_{off}) produced by our microscopic models are necessary to facilitate quantitative comparisons with experiment and with simulations across all resolutions. We show here that the time-dependent rates for the full model (Figure 1) are well-approximated by the analytical solutions when we use $D_{tot} = D_{eff}$, in both 3D and 2D (Figure 6). These results further highlight the impact that rotational diffusion can have on the kinetics of association for diffusion-controlled reactions such as the one studied here ($k_a = 166.9$ nm$^3/\mu$s $= 1.01 \times 10^8$ M^{-1} s^{-1}). As the motion changes from $D_t = 6$ to $D_{eff} = 12.66$ nm$^2/\mu$s due to rotational diffusion, the steady-state rate increases from 51.9 to a predicted value of 81.5 nm$^3/\mu$s (Figure 6a). The true rate (Figure 6a black diamonds) approaches an asymptotic value in 3D of 78.7 nm$^3/\mu$s, quite close to the predicted value.

In 2D, we again see that the kinetics for this diffusion-controlled reaction is clearly impacted significantly by rotational diffusion. The predicted rate using $D_{eff} = 6$ nm$^2/\mu$s is in excellent agreement with the numerical solution for $t <$ 100 μs, after which the true rate decays more rapidly (Figure 6b). This is not particularly surprising, given that, for diffusion-controlled reactions in 2D, reactions remain sensitive to spatial distributions over all times.[51] At longer times, particles are broadly distributed in space and their ability to find each other to produce a reactive collision will be limited by their translational diffusion, which in this case is 6 times slower than D_{eff}. Finally, it is worth noting that if the binding is rate-limited (e.g., $k_a/D < 0.5$ in 2D),[51] the kinetics in 3D or 2D will be insensitive to any changes to diffusion constants, including the addition of rotational diffusion.

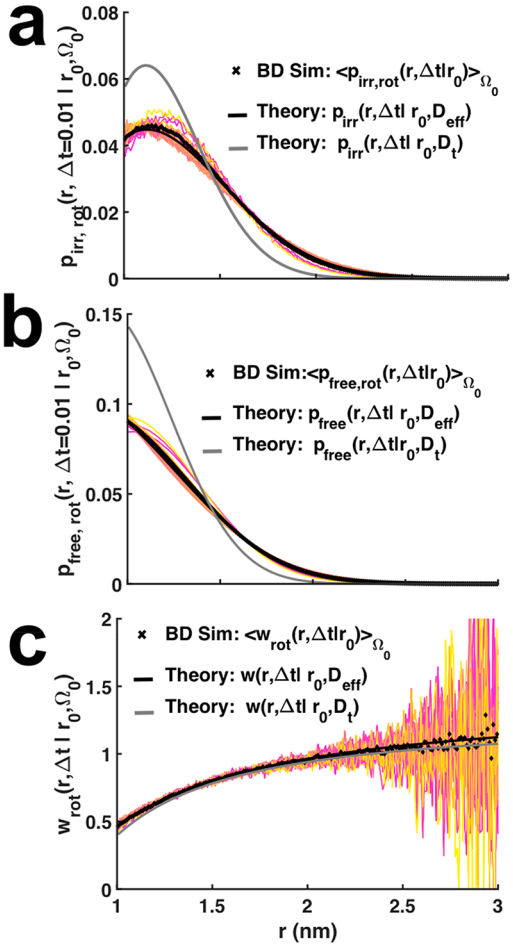

Figure 5. Green's Function (GFs) solutions for two rotating and translating reactive sites well approximated by use of D_{eff}. GFs are plotted here as a function of the final separation r at time $\Delta t = 0.01$ μs. All final orientations are averaged over. The initial separation is fixed at $r_0 = r_\sigma = 1$ nm for all curves, and each colorful curve corresponds to a distinct initial orientation $\Omega_0 = [\theta_{A0}, \theta_{B0}, \psi_0]$. The average over all initial orientations is shown in black × marks. Both theory curves show the GF predicted from the simpler analytical model of eq 2. (a) The GF with RBC. (b) GF for free diffusion with excluded volume enforced ($r \geq \sigma$) and the GF renormalized to one over $r \geq \sigma$. (c) Ratio of the GF in (a) relative to (b) used for reweighting in the FPR algorithm (Supporting Information).

4.3. Many-Body Equilibrium for Rotating Sites. Thus far, we have only studied reaction dynamics between a single pair of reactive molecules. Here, we simulate a pseudo-first-order reversible reaction, A + B ⇌ C, to carefully quantify the equilibrium values produced by our structure-resolved RD model (Figure 7). We simulate our dynamics using the FPR

DOI: 10.1021/acs.jpcb.8b08339
J. Phys. Chem. B 2018, 122, 11771−11783

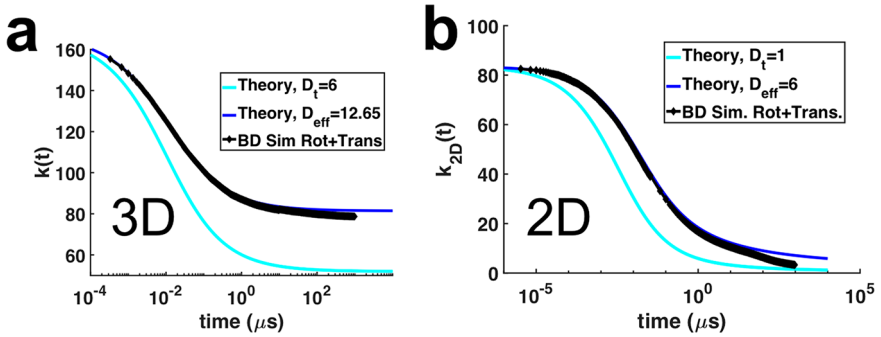

Figure 6. Kinetic rates of association are predicted by the translational model with D_{eff}. The time-dependent rate for the full model (black diamonds) can be calculated from BD simulations via the survival probabilities using, similar to eq 5, $k(t) = k_a \int\int\int \mathrm{d}\cos(\theta_A)\, \mathrm{d}\cos(\theta_B)\, \mathrm{d}\psi\, S(t|\sigma,\theta_A,\theta_B,\psi)$. Theory shows $k(t)$ calculated from eq 5 where $D_{tot} = D_t$ (cyan) or $D_{tot} = D_{eff}$ (blue). (a) In 3D, at t = 1 ms, the theoretical rate has nearly reached its steady state (81.6 versus k_{on} = 81.5 nm^3/μs), and the observed rate is 78.7. (b) In 2D, the rate decays logarithmically toward zero. One molecule translates with D_t = 1 nm^2/μs, and both molecules rotate around the z-axis with D_R = 0.05 rad^2/μs. k_a = 83.45 nm^2/μs.

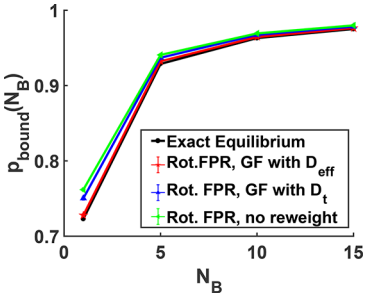

Figure 7. Equilibrium is correctly produced by our rotational FPR simulations for A + B ⇌ C. A central rotating A molecule binds reversibly to N_B rotating B molecules in a volume of V = (400 nm)^3. All particles have a center of mass site located l = 10 nm from the reactive sites. Error bars indicating standard error of mean (SEM) are smaller than the marker size. The exact solution is in black (eq 19). FPR simulations that evaluate reaction probabilities using D_{eff} (red) have percent errors of 0.69% for N = 1, 0.38% for N = 5, 0.15% for N = 10, and 0.14% for N = 15. The error increases about 3-fold if D_t is used instead (blue): 3.8% for N = 1, 0.89% for N = 5, 0.44% for N = 10, and 0.33% for N = 15. If D_t is used without any reweighting applied (green), errors increase to 5.4% for N = 1, 1.3% for N = 5, 0.65% for N = 10, and 0.5% for N = 15.

algorithm,[50,51] where particle positions are updated according to both translational and rotational Brownian motion (Supporting Information). We stress that the dynamics is always properly updated using D_t for translational updates to positions, and D_R for rotational updates to sites. We use D_{eff} only to evaluate reaction probabilities and their reweighting factors (Supporting Information). Simulations here used Δt = 0.1 μs, with nearly identical results produced for Δt = 0.5 μs. The equilibrium behavior is, as usual, independent of the dynamics or transport properties of the system, and the correct probability of the central A particle being bound to a B particle is given by

$$p_{bound} = \frac{K_{eq}B_0}{1 + K_{eq}B_0} \tag{19}$$

where $K_{eq} = k_a/k_b$ = 1.669 × 10^8 nm^3. The error of our simulations relative to the exact values is <1% for all system sizes (Figure 7). Each trajectory (N_{traj} = 20) produces at least 3000 binding events to converge the value of p_{bound}.

FPR simulations that simply used D_t to evaluate reaction probabilities and reweighting factors were less accurate, particularly for N_B = 1 (Figure 7). To recover exact association rates in FPR, reaction probabilities must be reweighted by the GFs (Figure 5c), and without reweighting applied, the error further increases. For all cases, the error does decrease as $N_B \gg N_A$. This suggests that a large field of binding partners could help cancel out the dependence of binding equilibrium on the shape of the reaction probability functions (e.g., Figure 4), as results using D_t only were still relatively accurate. However, as we will see below, the kinetics of association are also sensitive to the D used for evaluating reaction probabilities.

4.4. Many-Body Kinetics of Reversibly Binding, Rotating Sites. The kinetics of many-body association are

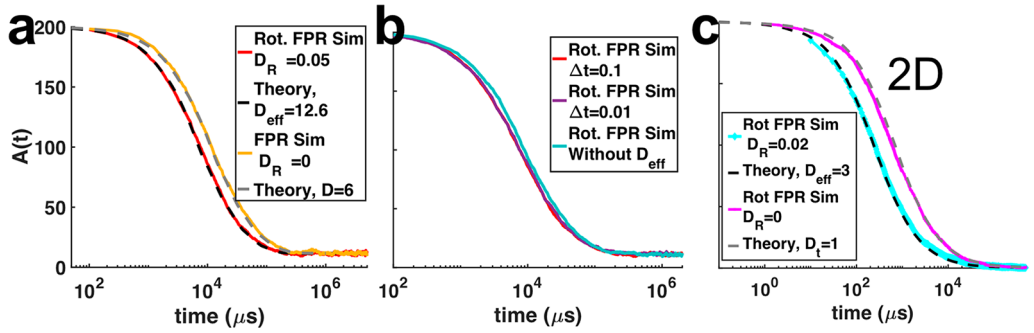

Figure 8. Rotational diffusion accelerates the kinetics of many-body association A + A ⇌ C for the diffusion-controlled rate of k_a = 166.9 nm^3/μs (1.01 × 10^8 M^{-1} s^{-1}). (a), (b) For each A molecule, D_t = 3 nm^2/μs and l = 10 nm. k_b = 1/s. A_{total} = 200 legs. Theoretical comparisons use the MRE (eq 20). (c) In 2D, D_t = 0.5 nm^2/μs.

DOI: 10.1021/acs.jpcb.8b08339
J. Phys. Chem. B 2018, 122, 11771−11783

also accurately captured by our rotational FPR simulations (Figure 8). We have simulated reversible association of 200 A molecules that rotate and translate, in both 3D (Figure 8a,b) and 2D (Figure 8c). For comparison, we solved for the time dependence of this reaction (A + A ⇌ C) using a very good theoretical solution provided via the modified rate equation (MRE):[79]

$$\frac{dA(t)}{dt} = -k(t)\,A(t)^2 + K_D k(t)\,C(t) \tag{20}$$

We solve this ODE numerically in MATLAB where the rate $k(t|k_a,\sigma,D_{tot})$ (eq 5) is solved either for rotation using $D_{tot} = D_{eff}$ or with no rotation, $D_{tot} = 2D_t$.

In Figure 8a,c one can clearly see that the introduction of rotational diffusion has accelerated the kinetics of association, while producing the same equilibrium. We verify that the size of the time step (0.01 or 0.1 μs) does not alter the kinetics or equilibrium of our simulations (Figure 8b red and purple). Changing the time step offers a stringent test for the method, as it changes the magnitude and shape of the reaction probabilities and the GFs in a nonlinear way. Figure 8b also shows how FPR simulations that evaluate reaction probabilities using only D_t instead of D_{eff} does produce error in the kinetics—it agrees with neither the proper rotational diffusion simulations nor the translational-only simulations.

4.5. Gillespie Simulations of Clathrin Trimer Self-Assembly. As a comparison to our structure-resolved RD simulations of clathrin trimer self-assembly (Figure 9), we used another rate-based approach, the nonspatial Gillespie algorithm with rule-based interactions, where each clathrin molecule has three sites (Supporting Information). As expected, the Gillespie simulations recover the precise equilibrium and kinetics of an A + A ⇌ C reaction for all simulations, as structure and geometry do not influence interactions. Importantly, we define the macroscopic rates for Gillespie simulations on the basis of the microscopic parameters of the RD model (Methods, with $D_{tot} = D_{eff}$) to ensure maximal similarity. With 100 trimers, there are 300 legs or A molecules, and for K_D = 100, 1, and 0.2 μM, the equilibrium number of bound leg pairs (C_{eq}) are thus 10.7, 106.1, and 128.4 respectively, as shown in Figure 10.

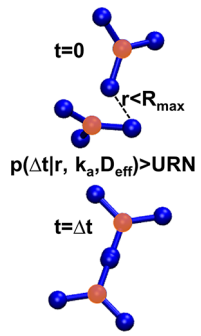

Figure 9. Model of clathrin trimer geometry and bound structure. Each rigid trimer has three reactive sites indicated in blue, located 10 nm from the center site shown in orange. If two reactive sites are within collision distance for the time step, $r < R_{max}$ (Supporting Information), they associate if the reaction probability is greater than a uniform random number (URN), regardless of the orientation. Once association occurs, however, the trimers are "snapped" into place to impose a planar complex geometry. Each binding site has excluded volume relative to all other open sites (e.g., they either react or reflect off of each other), and the "legs" and the center of mass particles have no volume.

4.6. Structure-Resolved RD Simulations of Clathrin Trimer Self-Assembly. A powerful aspect of our new approach is that it can be applied to studying self-assembly of rotating sites that are part of a rigid complex, such as a model of a clathrin trimer (Figure 9). While still simulating an A + A ⇌ C reaction, we can quantify how rigid structure, space, and diffusion affect complex formation and assembly, with direct comparison to the Gillespie simulations of the same systems. In this simplified model of a clathrin trimer, the three reactive sites are arranged in a plane with 120° between them, 10 nm from the center. Each bound pair are "snapped" into place in a plane (Figure 9) to mimic the experimental structures of clathrin lattices that form plaques on the membrane.[80]

For weak binding (K_D = 100 μM), we find that the structure-resolved RD simulations produce the same equilibrium and kinetics as the Gillespie simulations (Figure 10a). This is expected, because when limited numbers of complexes form, hexagons will not form and structure does not impact kinetics. We also verify that the RD results are the same for two different time steps (0.1 and 0.01 μs), producing equilibrium bound pairs of 10.9 ± 0.65 (SEM) for 0.1 μs and 10.6 ± 0.5 for 0.01 μs, in good agreement with the exact value of 10.7.

For stronger binding, however, the structure-resolved RD simulations differ even at equilibrium for two main reasons. One reason is that, as large complexes form, the spatial geometry prevents specific pairs of legs from being able to bind, even if they are free. For a perfect tiling of the 100 trimers we simulate here, the global optimum has 38 closed hexagons, 137 bound pairs, and 26 legs unbound (Supporting Information). This feature cannot be captured in Gillespie simulations, as the rules apply to pairs of molecules and any extension to specific complex geometries (e.g., 6-mers forming hexagons) becomes combinatorially prohibitive. However, even with K_D = 0.2 μM, the equilibrium bound legs of 128.4 is below this maximum threshold of 137, so it is not the largest source of deviations between the two simulations.

The second and more significant reason that the RD simulations differ from the Gillespie is because the trimeric clathrin molecules form closed hexagonal loops (Figure 10b inset). A closed hexagon has six bound pairs, but once the fifth pair is bound, the final two free sites are at contact and are part of the same complex. This means that they are no longer diffusing relative to one another. The reaction probability (eq 3) approaches 1 as $D \to 0$ if particles are at contact ($r = \sigma$), and approaches 0 otherwise, independently of the rate. We therefore define the probability of this hexagon (or loop) closure in two ways. In one case, we set the probability of hexagon closure to 1, which means the hexagon formation is irreversible and the simulations remain nonequilibrium. In the other case, we defined a probability of hexagon closure that would preserve detailed balance (DB) and allow for dynamic remodeling of the hexagons at equilibrium (Supporting Information).

As seen in Figure 10b,c, in the irreversible hexagon closure simulations (magenta), we see a slow but steady growth in legs bound as lattices anneal and become locked into place. A snapshot from one of these simulation trajectories is shown in Figure 11c, where the lattice shown formed after 10.5 s at K_D = 0.2 μM and is effectively frozen in this configuration. For the DB simulations, the time when the first hexagons form agrees

DOI: 10.1021/acs.jpcb.8b08339
J. Phys. Chem. B 2018, 122, 11771−11783

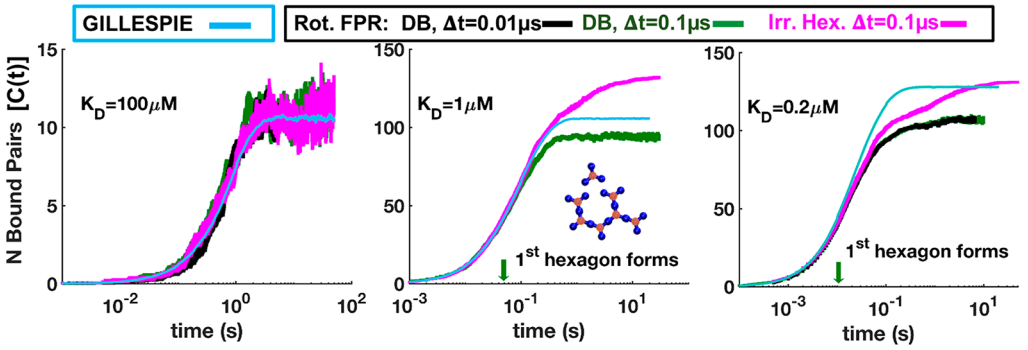

Figure 10. Kinetics of clathrin trimer self-assembly changes with structural constraints for stronger binding interactions. For Gillespie simulations (blue) the kinetics is simply given by A + A ⇌ C where total $N_A = 3N_{trimers}$, and $k_{off} = 1\ s^{-1}$ for all simulations. $C(t)$ is plotted versus time. Rotational FPR simulations (black, $\Delta t = 0.01\ \mu s$; green, 0.1 μs; magenta, 0.1 μs) shown with error bars indicating SEM over 20 trajectories. The three distinct models (blue vs magenta vs black/green) begin to diverge from each other after hexagons start forming, as indicated by the green arrow.

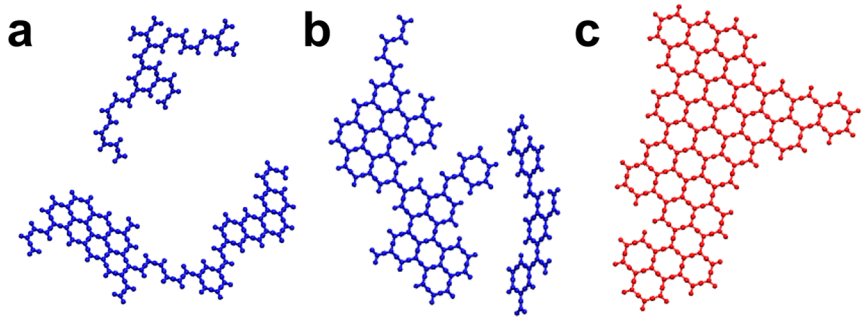

Figure 11. Clathrin lattice formation in solution remodels dynamically with reversible hexagon closure. (a), (b) Snapshots from a single trajectory with $K_D = 0.2\ \mu M$ and $\Delta t = 0.1\ \mu s$, where we enforce detailed balance (DB) for closure of the hexagons and the lattice dynamically remodels. (c) Here again $K_D = 0.2\ \mu M$, but the hexagon closure is irreversible. Once the structure shown has formed at 10.5 s, all 100 trimers are incorporated and no dissociation event will allow a trimer to diffuse away (Movie S2).

with the irreversible hexagon simulations, and prior to these events, the kinetics of both these RD simulations agree relatively closely with the Gillespie simulations (Figure 10b,c). However, the subsequent kinetics diverge as hexagon formation increases. The frequency of these hexagon closure events is ultimately lower in the DB simulations than that produced by free association, driving down the total number of bound legs at equilibrium relative to what is seen from Gillespie simulations. These results illustrate how the definition of hexagon closure probability has quantitative and qualitative impact on the equilibrium and dynamics of the lattice assembly (Figure 11, Movie S1). Loop closure was also found to be a critical parameter controlling the self-assembly of receptors on the cell surface.[61] From our DB simulations, we calculated the average number of hexagons closed at equilibrium to be 0 for 100 μM, 2.5 ± 1.6 for 1 μM (±here is standard deviation), and 8.5 ± 3.3 for 0.2 μM. In contrast, for the irreversible hexagon simulations, the average numbers of closed hexagons are 0.05 ± 0.2 for 100 μM, 33 ± 2.4 for 1 μM, and 31 ± 2 for 0.2 μM, as calculated at the end of the simulations.

Finally, we note that the early kinetics of the RD simulations is very similar to the Gillespie simulation kinetics (Figure 10), in large part because the systems start out well-mixed and the binding is not diffusion controlled for monomer and small oligomer binding events. In particular, even for $K_D = 0.2\ \mu M$, the macroscopic rate in the Gillespie simulations is $k_{on} = 5 \times 10^6\ M^{-1}\ s^{-1}$. For the corresponding RD simulations, this macroscopic rate results from both the diffusional search time and the rate of binding once at contact (eq 6), and the diffusional rate is ∼10 times faster than the binding rate at contact, thus minimally impacting the overall kinetics. Once larger structures attempt to bind, however, diffusion can slow down rates of association, as larger complexes have smaller diffusion constants (Methods). Binding of larger complexes (e.g., Figure 11) can also produce steric overlap, and these moves must be rejected, further contributing to slower kinetics. The RD kinetics is accelerated only in the event of hexagon closure. This reaction is instantaneous for the irreversible model, due to the spatial localization of the sites.

5. DISCUSSION

5.1. Application to Other Single-Particle RD Methods.

Single-particle RD approaches[50−56] typically use simple Brownian updates to particle positions based on free diffusion, and rotation can be straightforwardly added in by performing Euler rotations. Whether the method is KMC or GF based, the reaction probabilities of association can be evaluated using their existing functional forms but parametrized by D_{eff} rather than D_t. The ability of these rigid-body simulations to create large assemblies, however, does introduce new demands on RD software. Additional bookkeeping is needed to ensure that protein complexes move as a rigid unit and that dissociation events only separate the two molecules that unbind. This issue is computational rather than algorithmic and must be confronted in any rule-based method that tracks multiprotein complex formation (e.g., BioNetGen[38]). Association events

DOI: 10.1021/acs.jpcb.8b08339
J. Phys. Chem. B 2018, 122, 11771−11783

between multiprotein structures, such as the clathrin lattices simulated here, can also produce steric overlap which should be prevented. In our software, we evaluate possible overlap in all newly formed complexes, rejecting events that produce nonphysical, overlapping sites, similar to previous work studying receptor binding on surfaces.[61] Additionally, the specific geometry of a multisite molecule could lead to a reduced macroscopic rate relative to the predicted value (Supporting Information). If repeated reactive sites are densely packed on a molecule, they can partially occlude access to binding, as previous work on cell surface receptors has shown.[81] For our clathrin molecule this is not an issue, but it is an important consideration for comparing kinetics across macroscopic and microscopic models.

The addition of multiple sites to a single rigid molecule also produces correlated motion, which is physically reasonable for a protein with multiple binding interfaces. However, in most single-particle RD methods, the evaluation of reaction probabilities and of diffusional position updates for each reaction site is assumed to be independent of all other sites except (at most) a single reaction partner within a time step. Once a rigid molecule has to avoid overlap due to one of its sites, this position update for the other sites deviates from the exact propagator. Ultimately, this coupling cannot be totally eliminated. However, it is minimized by taking smaller time steps. With smaller steps, each site will have fewer possible partners to react with, and the assumption that only one collision could occur for each *rigid molecule* (not each reactive site) will be better maintained. Verifying that observed kinetics are preserved at smaller time steps, as we did above, is thus an important test of method and model accuracy. We have found that these errors in the expected positional distributions of reactive pairs has a rather small impact on kinetics of many-body association. This is likely because in many-body diffusing systems, random positional errors occur in all directions and tend to even out.

5.2. Limitations and Future Directions. An important limitation of our model is that binding reactions are not dependent on molecular orientation. For small globular proteins, where the hydrodynamic radius is ∼2 nm, this is a minor concern, as rotational diffusion is fast (from Einstein–Stokes D_R = 21 rad^2/μs) and, over the course of a 0.1 μs time step, will have nearly uniformly sampled orientations (see, e.g., eq 11). However, for larger structures, slow rotation means that orientational constraints can have more control on aligning structures over these microsecond time scales. The more artificial and practical side of this approximation is that larger structures can bind from any orientation relative to one another, as long as their binding sites are close together. These association events that create large displacements could be rejected, similar to events that create steric overlap. Our simple model of association also neglects the effects of electrostatics[82] or hydrodynamics[83] on controlling association because of their computational expense, although they are compatible with the FPR algorithm.[50] Protein flexibility is also important for binding interactions involving multivalent intrinsically disordered proteins, and integration of our model with the approach of Spring SALAD[75] would be a promising future method for modeling these proteins.

5.3. RD Simulations of Clathrin Lattice Assembly. Recent energy-function-based models have successfully studied clathrin lattice and cage assembly, and while these models are coarse-grained (CG) from the perspective of molecular dynamics, they are higher resolution than our model because of their ability to capture orientational effects[15,20] and flexibility.[19] However, an RD model such as ours has advantages for modeling CME in the cell. First, CG interactions for large molecules such as clathrin are quite specific for each system studied, as is the software, which makes them difficult to transfer from one system to another. Energy-function-based models each have a distinct definition of clathrin interactions and geometry, whereas our rate-based RD model is adaptable to various software tools. Second, specifying and parametrizing additional CG interactions for clathrin with the dozens of additional proteins that are known to mediate CME in the cell is not practical. In contrast, because binding constants and structures are known for many of the CME protein–protein interactions, they can be directly used in rate-based models.[43,60] Finally, rate-based approaches can readily be applied to studying nonequilibrium processes such as CME. In a recent nonspatial rate-based model of clathrin assembly involving eight different protein types, we demonstrated that the stoichiometry of adaptor proteins and the strength of their interactions with clathrin, as measured experimentally, control the localization of clathrin to the membrane and the speed and success of assembly into vesicles.[43]

Our structurally resolved clathrin model simulated here builds in the sterics and geometric constraints missing from our nonspatial rate-based model of clathrin vesicle formation.[43] We found here that dynamic remodeling of the clathrin lattice was sensitive to not only the trimer–trimer binding constant but also the rate of hexagonal loop closure in the lattice. As a result, the kinetics and steady-state behavior of clathrin lattice assembly differed from what was expected from a nonspatial rate-based simulation once hexagons started to form. Experimental estimates of clathrin-clathrin dimerization indicate weak stability, with a K_D of ∼115 μM.[84] Using a similar value of 100 μM (Figure 10a), our clathrin model does not assemble lattices in solution, as is observed physiologically.[85] Although we simulated flat lattices here, which are only observed to form on membranes, in future work the structure of the rigid clathrin can be "puckered" to assemble into closed cages. As this paper focuses on the ability to generally simulate structure-resolved RD, we will perform a more thorough characterization of clathrin assembly kinetics, including on the membrane (2D), in a future work.

6. CONCLUSIONS

Molecular modeling approaches are well-established for simulating self-assembly but are not capable of reaching the slow time scales of the cellular process or capturing their frequent dependence on chemical reactions such as phosphorylation. However, single-particle reaction diffusion is amenable to simulating chemical reactions and reaching the long slow time scales of cellular processes. Our structure-resolved RD method presented here is a first approach for combining these features to study self-assembly in the cell. The method was demonstrated here on the clathrin lattice assembly but is general enough to be used on a range of multicomponent self-assembly problems in solution and on the membrane. The method is simple enough to be incorporated into single-particle RD software, and our code is freely available on github.com/mjohn218/FPR_rot. We are developing user-friendly software tools to facilitate the setup and simulation of rate-based RD systems of self-assembly.

DOI: 10.1021/acs.jpcb.8b08339
J. Phys. Chem. B 2018, 122, 11771–11783

■ ASSOCIATED CONTENT

Supporting Information

The Supporting Information is available free of charge on the ACS Publications website at DOI: 10.1021/acs.jpcb.8b08339.

Further details on simulation methods and optimal hexagonal tiling (PDF)

Structure-resolved RD simulation of clathrin trimers with DB hexagon closure, K_D = 0.2 μM, 5 ms between frames (MPG)

Structure-resolved RD simulation of clathrin trimers with irreversible hexagon closure, K_D = 0.2 μM, 10 ms between frames (MPG)

■ AUTHOR INFORMATION

Corresponding Author

*E-mail: margaret.johnson@jhu.edu.

ORCID

Margaret E. Johnson: 0000-0001-9881-291X

Notes

The author declares no competing financial interest.

■ ACKNOWLEDGMENTS

Research reported in this publication was supported by the National Institute of General Medical Sciences of the NIH under Award No. R00GM098371 to M.E.J. The content is solely the responsibility of the authors and does not necessarily represent the official view of the NIH. The research used the NSF XSEDE computational resources of SuperMic under XRAC MCB150059, and the MARCC supercomputer at JHU. We thank Dr. Matthew Varga for helpful comments on the manuscript. We thank Dr. Osman N. Yogurtcu for simulations verifying the accuracy and convergence of the Brownian Dynamics simulations.

■ REFERENCES

(1) Avinoam, O.; Schorb, M.; Beese, C. J.; Briggs, J. A.; Kaksonen, M. Endocytosis. Endocytic Sites Mature by Continuous Bending and Remodeling of the Clathrin Coat. *Science* **2015**, *348*, 1369−1372.

(2) Dores, M. R.; Chen, B.; Lin, H.; Soh, U. J. K.; Paing, M. M.; Montagne, W. A.; Meerloo, T.; Trejo, J. Alix Binds a Ypx3l Motif of the Gpcr Par1 and Mediates Ubiquitin-Independent Escrt-Iii/Mvb Sorting. *J. Cell Biol.* **2012**, *197*, 407−419.

(3) Wu, H. Higher-Order Assemblies in a New Paradigm of Signal Transduction. *Cell* **2013**, *153*, 287−292.

(4) Votteler, J.; Sundquist, Wesley I. Virus Budding and the Escrt Pathway. *Cell Host Microbe* **2013**, *14*, 232−241.

(5) Hagan, M. F. Modeling Viral Capsid Assembly. *Adv. Chem. Phys.* **2014**, *155*, 1−68.

(6) Grime, J. M.; Voth, G. A. Early Stages of the Hiv-1 Capsid Protein Lattice Formation. *Biophys. J.* **2012**, *103*, 1774−1783.

(7) Grime, J. M.; Dama, J. F.; Ganser-Pornillos, B. K.; Woodward, C. L.; Jensen, G. J.; Yeager, M.; Voth, G. A. Coarse-Grained Simulation Reveals Key Features of Hiv-1 Capsid Self-Assembly. *Nat. Commun.* **2016**, *7*, 11568.

(8) Qiao, X.; Jeon, J.; Weber, J.; Zhu, F.; Chen, B. Mechanism of Polymorphism and Curvature of Hiv Capsid Assemblies Probed by 3d Simulations with a Novel Coarse Grain Model. *Biochim. Biophys. Acta, Gen. Subj.* **2015**, *1850*, 2353−2367.

(9) Johnston, I. G.; Louis, A. A.; Doye, J. P. Modelling the Self-Assembly of Virus Capsids. *J. Phys.: Condens. Matter* **2010**, *22*, 104101.

(10) Elrad, O. M.; Hagan, M. F. Encapsulation of a Polymer by an Icosahedral Virus. *Phys. Biol.* **2010**, *7*, 045003.

(11) Perlmutter, J. D.; Mohajerani, F.; Hagan, M. F. Many-Molecule Encapsulation by an Icosahedral Shell. *eLife* **2016**, *5*, e14078.

(12) Damasceno, P. F.; Engel, M.; Glotzer, S. C. Predictive Self-Assembly of Polyhedra into Complex Structures. *Science* **2012**, *337*, 453−457.

(13) Fonseca, P.; Romano, F.; Schreck, J. S.; Ouldridge, T. E.; Doye, J. P. K.; Louis, A. A. Multi-Scale Coarse-Graining for the Study of Assembly Pathways in DNA-Brick Self-Assembly. *J. Chem. Phys.* **2018**, *148*, 134910.

(14) Fotin, A.; Cheng, Y.; Sliz, P.; Grigorieff, N.; Harrison, S. C.; Kirchhausen, T.; Walz, T. Molecular Model for a Complete Clathrin Lattice from Electron Cryomicroscopy. *Nature* **2004**, *432*, 573−579.

(15) den Otter, W. K.; Renes, M. R.; Briels, W. J. Asymmetry as the Key to Clathrin Cage Assembly. *Biophys. J.* **2010**, *99*, 1231−1238.

(16) Giani, M.; den Otter, W. K.; Briels, W. J. Clathrin Assembly Regulated by Adaptor Proteins in Coarse-Grained Models. *Biophys. J.* **2016**, *111*, 222−235.

(17) Giani, M.; den Otter, W. K.; Briels, W. J. Early Stages of Clathrin Aggregation at a Membrane in Coarse-Grained Simulations. *J. Chem. Phys.* **2017**, *146*, 155102.

(18) Matthews, R.; Likos, C. N. Influence of Fluctuating Membranes on Self-Assembly of Patchy Colloids. *Phys. Rev. Lett.* **2012**, *109*, 178302.

(19) Matthews, R.; Likos, C. N. Structures and Pathways for Clathrin Self-Assembly in the Bulk and on Membranes. *Soft Matter* **2013**, *9*, 5794−5806.

(20) Schoen, A. P.; Cordella, N.; Mehraeen, S.; Arunagirinathan, M. A.; Spakowitz, A. J.; Heilshorn, S. C. Dynamic Remodelling of Disordered Protein Aggregates Is an Alternative Pathway to Achieve Robust Self-Assembly of Nanostructures. *Soft Matter* **2013**, *9*, 9137−9145.

(21) Glaser, J.; Nguyen, T. D.; Anderson, J. A.; Lui, P.; Spiga, F.; Millan, J. A.; Morse, D. C.; Glotzer, S. C. Strong Scaling of General-Purpose Molecular Dynamics Simulations on Gpus. *Comput. Phys. Commun.* **2015**, *192*, 97−107.

(22) Romano, F.; De Michele, C.; Marenduzzo, D.; Sanz, E. Monte Carlo and Event-Driven Dynamics of Brownian Particles with Orientational Degrees of Freedom. *J. Chem. Phys.* **2011**, *135*, 124106.

(23) Ilie, I. M.; den Otter, W. K.; Briels, W. J. Rotational Brownian Dynamics Simulations of Clathrin Cage Formation. *J. Chem. Phys.* **2014**, *141*, 065101.

(24) Zhang, Z.; Glotzer, S. C. Self-Assembly of Patchy Particles. *Nano Lett.* **2004**, *4*, 1407−1413.

(25) Gabdoulline, R. R.; Wade, R. C. Protein-Protein Association: Investigation of Factors Influencing Association Rates by Brownian Dynamics Simulations. *J. Mol. Biol.* **2001**, *306*, 1139−1155.

(26) Mereghetti, P.; Gabdoulline, R. R.; Wade, R. C. Brownian Dynamics Simulation of Protein Solutions: Structural and Dynamical Properties. *Biophys. J.* **2010**, *99*, 3782−3791.

(27) Ermak, D. L.; Mccammon, J. A. Brownian Dynamics with Hydrodynamic Interactions. *J. Chem. Phys.* **1978**, *69*, 1352−1360.

(28) Elcock, A. H.; Sept, D.; McCammon, J. A. Computer Simulation of Protein-Protein Interactions. *J. Phys. Chem. B* **2001**, *105*, 1504−1518.

(29) Levandovsky, A.; Zandi, R. Nonequilibirum Assembly, Retroviruses, and Conical Structures. *Phys. Rev. Lett.* **2009**, *102*, 198102.

(30) Gillespie, D. T. Exact Stochastic Simulation of Coupled Chemical Reactions. *J. Phys. Chem.* **1977**, *81*, 2340−2361.

(31) Gillespie, D. T. General Method for Numerically Simulating Stochastic Time Evolution of Coupled Chemical-Reactions. *J. Comput. Phys.* **1976**, *22*, 403−434.

(32) Hlavacek, W. S.; Faeder, J. R.; Blinov, M. L.; Posner, R. G.; Hucka, M.; Fontana, W. Rules for Modeling Signal-Transduction Systems. *Sci. Signaling* **2006**, *2006*, re6.

(33) Thomas, M.; Schwartz, R. Quantitative Computational Models of Molecular Self-Assembly in Systems Biology. *Phys. Biol.* **2017**, *14*, 035003.

(34) Smith, G. R.; Xie, L.; Lee, B.; Schwartz, R. Applying Molecular Crowding Models to Simulations of Virus Capsid Assembly in Vitro. *Biophys. J.* **2014**, *106*, 310−320.
(35) Endres, D.; Zlotnick, A. Model-Based Analysis of Assembly Kinetics for Virus Capsids or Other Spherical Polymers. *Biophys. J.* **2002**, *83*, 1217−1230.
(36) Zlotnick, A. To Build a Virus Capsid. An Equilibrium Model of the Self Assembly of Polyhedral Protein Complexes. *J. Mol. Biol.* **1994**, *241*, 59−67.
(37) Gruenert, G.; Ibrahim, B.; Lenser, T.; Lohel, M.; Hinze, T.; Dittrich, P. Rule-Based Spatial Modeling with Diffusing, Geometrically Constrained Molecules. *BMC Bioinf.* **2010**, *11*, 307.
(38) Faeder, J. R.; Blinov, M. L.; Hlavacek, W. S. Rule-Based Modeling of Biochemical Systems with Bionetgen. *Methods Mol. Biol.* **2009**, *500*, 113−167.
(39) Smith, A. M.; Xu, W.; Sun, Y.; Faeder, J. R.; Marai, G. E. Rulebender: Integrated Modeling, Simulation and Visualization for Rule-Based Intracellular Biochemistry. *BMC Bioinf.* **2012**, *13* (Suppl 8), S3.
(40) Sneddon, M. W.; Faeder, J. R.; Emonet, T. Efficient Modeling, Simulation and Coarse-Graining of Biological Complexity with Nfsim. *Nat. Methods* **2011**, *8*, 177−U112.
(41) Sweeney, B.; Zhang, T.; Schwartz, R. Exploring the Parameter Space of Complex Self-Assembly through Virus Capsid Models. *Biophys. J.* **2008**, *94*, 772−783.
(42) Zhang, T.; Schwartz, R. Simulation Study of the Contribution of Oligomer/Oligomer Binding to Capsid Assembly Kinetics. *Biophys. J.* **2006**, *90*, 57−64.
(43) Holland, D. O.; Johnson, M. E. Stoichiometric Balance of Protein Copy Numbers Is Measurable and Functionally Significant in a Protein-Protein Interaction Network for Yeast Endocytosis. *PLoS Comput. Biol.* **2018**, *14*, e1006022.
(44) Moraru, I. I.; Schaff, J. C.; Slepchenko, B. M.; Blinov, M. L.; Morgan, F.; Lakshminarayana, A.; Gao, F.; Li, Y.; Loew, L. M. Virtual Cell Modelling and Simulation Software Environment. *IET Syst. Biol.* **2008**, *2*, 352−362.
(45) Angermann, B. R.; Klauschen, F.; Garcia, A. D.; Prustel, T.; Zhang, F.; Germain, R. N.; Meier-Schellersheim, M. Computational Modeling of Cellular Signaling Processes Embedded into Dynamic Spatial Contexts. *Nat. Methods* **2012**, *9*, 283−289.
(46) Roberts, E.; Stone, J. E.; Luthey-Schulten, Z. Lattice Microbes: High-Performance Stochastic Simulation Method for the Reaction-Diffusion Master Equation. *J. Comput. Chem.* **2013**, *34*, 245−255.
(47) Sanft, K. R.; Wu, S.; Roh, M.; Fu, J.; Lim, R. K.; Petzold, L. R. Stochkit2: Software for Discrete Stochastic Simulation of Biochemical Systems with Events. *Bioinformatics* **2011**, *27*, 2457−2458.
(48) Drawert, B.; Hellander, S.; Trogdon, M.; Yi, T. M.; Petzold, L. A Framework for Discrete Stochastic Simulation on 3d Moving Boundary Domains. *J. Chem. Phys.* **2016**, *145*, 184113.
(49) Drawert, B.; Engblom, S.; Hellander, A. Urdme: A Modular Framework for Stochastic Simulation of Reaction-Transport Processes in Complex Geometries. *BMC Syst. Biol.* **2012**, *6*, 76.
(50) Johnson, M. E.; Hummer, G. Free-Propagator Reweighting Integrator for Single-Particle Dynamics in Reaction-Diffusion Models of Heterogeneous Protein-Protein Interaction Systems. *Phys. Rev. X* **2014**, *4*, 031037.
(51) Yogurtcu, O. N.; Johnson, M. E. Theory of Bi-Molecular Association Dynamics in 2d for Accurate Model and Experimental Parameterization of Binding Rates. *J. Chem. Phys.* **2015**, *143*, 084117.
(52) Takahashi, K.; Tanase-Nicola, S.; ten Wolde, P. R. Spatio-Temporal Correlations Can Drastically Change the Response of a Mapk Pathway. *Proc. Natl. Acad. Sci. U. S. A.* **2010**, *107*, 2473−2478.
(53) Gillespie, D. T.; Seitaridou, E.; Gillespie, C. A. The Small-Voxel Tracking Algorithm for Simulating Chemical Reactions among Diffusing Molecules. *J. Chem. Phys.* **2014**, *141*, 234115.
(54) Schoneberg, J.; Noe, F. Readdy - a Software for Particle-Based Reaction-Diffusion Dynamics in Crowded Cellular Environments. *PLoS One* **2013**, *8*, e74261.
(55) Kerr, R. A.; Bartol, T. M.; Kaminsky, B.; Dittrich, M.; Chang, J. C. J.; Baden, S. B.; Sejnowski, T. J.; Stiles, J. R. Fast Monte Carlo Simulation Methods for Biological Reaction-Diffusion Systems in Solution and on Surfaces. *Siam J. Sci. Comput* **2008**, *30*, 3126−3149.
(56) Andrews, S. S.; Addy, N. J.; Brent, R.; Arkin, A. P. Detailed Simulations of Cell Biology with Smoldyn 2.1. *PLoS Comput. Biol.* **2010**, *6*, e1000705.
(57) Kerr, R. A.; Levine, H.; Sejnowski, T. J.; Rappel, W. J. Division Accuracy in a Stochastic Model of Min Oscillations in Escherichia Coli. *Proc. Natl. Acad. Sci. U. S. A.* **2006**, *103*, 347−352.
(58) Jilkine, A.; Angenent, S. B.; Wu, L. F.; Altschuler, S. J. A Density-Dependent Switch Drives Stochastic Clustering and Polarization of Signaling Molecules. *PLoS Comput. Biol.* **2011**, *7*, e1002271.
(59) Paijmans, J.; Lubensky, D. K.; Ten Wolde, P. R. Period Robustness and Entrainability of the Kai System to Changing Nucleotide Concentrations. *Biophys. J.* **2017**, *113*, 157−173.
(60) Yogurtcu, O. N.; Johnson, M. E. Cytoplasmic Proteins Can Exploit Membrane Localization to Trigger Functional Assembly. *PLoS Comput. Biol.* **2018**, *14*, e1006031.
(61) Monine, M. I.; Posner, R. G.; Savage, P. B.; Faeder, J. R.; Hlavacek, W. S. Modeling Multivalent Ligand-Receptor Interactions with Steric Constraints on Configurations of Cell-Surface Receptor Aggregates. *Biophys. J.* **2010**, *98*, 48−56.
(62) Northrup, S. H.; Allison, S. A.; Mccammon, J. A. Brownian Dynamics Simulation of Diffusion-Influenced Bimolecular Reactions. *J. Chem. Phys.* **1984**, *80*, 1517−1526.
(63) Allison, S. A.; Srinivasan, N.; Mccammon, J. A.; Northrup, S. H. Diffusion-Controlled Reactions between a Spherical Target and Dumbell Dimer by Brownian Dynamics Simulation. *J. Phys. Chem.* **1984**, *88*, 6152−6157.
(64) Zhou, H. X. Brownian Dynamics Study of the Influences of Electrostatic Interaction and Diffusion on Protein-Protein Association Kinetics. *Biophys. J.* **1993**, *64*, 1711−1726.
(65) Zhou, H. X. Kinetics of Diffusion-Influenced Reactions Studied by Brownian Dynamics. *J. Phys. Chem.* **1990**, *94*, 8794−8800.
(66) Zhou, H. X.; Szabo, A. Theory and Simulation of the Time-Dependent Rate Coefficients of Diffusion-Influenced Reactions. *Biophys. J.* **1996**, *71*, 2440−2457.
(67) Vijaykumar, A.; Ouldridge, T. E.; Ten Wolde, P. R.; Bolhuis, P. G. Multiscale Simulations of Anisotropic Particles Combining Molecular Dynamics and Green's Function Reaction Dynamics. *J. Chem. Phys.* **2017**, *146*, 114106.
(68) von Smoluchowski, M. Attempt to Derive a Mathematical Theory of Coagulation Kinetics in Colloidal Solutions. *Z. Phys. Chem.* **1917**, *92*, 129.
(69) van Zon, J. S.; ten Wolde, P. R. Green's-Function Reaction Dynamics: A Particle-Based Approach for Simulating Biochemical Networks in Space and Time. *J. Chem. Phys.* **2005**, *123*, 234910.
(70) van Zon, J. S.; ten Wolde, P. R. Simulating Biochemical Networks at the Particle Level and in Time and Space: Green's Function Reaction Dynamics. *Phys. Rev. Lett.* **2005**, *94*, 128103.
(71) Andrews, S. S.; Bray, D. Stochastic Simulation of Chemical Reactions with Spatial Resolution and Single Molecule Detail. *Phys. Biol.* **2004**, *1*, 137−151.
(72) Andrews, S. S. Smoldyn: Particle-Based Simulation with Rule-Based Modeling, Improved Molecular Interaction and a Library Interface. *Bioinformatics* **2017**, *33*, 710−717.
(73) Rice, S. A. *Diffusion Limited Reactions*; Elsevier Science and Technology: Netherlands, 1985; Vol. *25*.
(74) Carslaw, H. S.; Jaeger, J. C. *Conduction of Heat in Solids*; Clarendon Press: Oxford, 1959.
(75) Michalski, P. J.; Loew, L. M. Springsalad: A Spatial, Particle-Based Biochemical Simulation Platform with Excluded Volume. *Biophys. J.* **2016**, *110*, 523−529.
(76) Collins, F. C.; Kimball, G. E. Diffusion-Controlled Reaction Rates. *J. Colloid Sci.* **1949**, *4*, 425−437.
(77) Shoup, D.; Lipari, G.; Szabo, A. Diffusion-Controlled Bimolecular Reaction-Rates - the Effect of Rotational Diffusion and Orientation Constraints. *Biophys. J.* **1981**, *36*, 697−714.

DOI: 10.1021/acs.jpcb.8b08339
J. Phys. Chem. B 2018, 122, 11771−11783

(78) Schlosshauer, M.; Baker, D. A General Expression for Bimolecular Association Rates with Orientational Constraints. *J. Phys. Chem. B* **2002**, *106*, 12079−12083.
(79) Szabo, A. Theoretical Approaches to Reversible Diffusion-Influenced Reactions: Monomer-Excimer Kinetics. *J. Chem. Phys.* **1991**, *95*, 2481.
(80) Heuser, J. Three-Dimensional Visualization of Coated Vesicle Formation in Fibroblasts. *J. Cell Biol.* **1980**, *84*, 560−583.
(81) Hlavacek, W. S.; Posner, R. G.; Perelson, A. S. Steric Effects on Multivalent Ligand-Receptor Binding: Exclusion of Ligand Sites by Bound Cell Surface Receptors. *Biophys. J.* **1999**, *76*, 3031−3043.
(82) Schreiber, G.; Haran, G.; Zhou, H. X. Fundamental Aspects of Protein-Protein Association Kinetics. *Chem. Rev.* **2009**, *109*, 839−860.
(83) Dlugosz, M.; Antosiewicz, J. M.; Zielinski, P.; Trylska, J. Contributions of Far-Field Hydrodynamic Interactions to the Kinetics of Electrostatically Driven Molecular Association. *J. Phys. Chem. B* **2012**, *116*, 5437−5447.
(84) Wakeham, D. E.; Chen, C. Y.; Greene, B.; Hwang, P. K.; Brodsky, F. M. Clathrin Self-Assembly Involves Coordinated Weak Interactions Favorable for Cellular Regulation. *EMBO J.* **2003**, *22*, 4980−4990.
(85) Pearse, B. M. F.; Crowther, R. A. Structure and Assembly of Coated Vesicles. *Annu. Rev. Biophys. Biophys. Chem.* **1987**, *16*, 49−68.

DOI: 10.1021/acs.jpcb.8b08339
J. Phys. Chem. B 2018, 122, 11771−11783